A Hybrid Regularizer Combining Orthonormal Wavelets and Finite Differences for Statistical Reconstruction in 3-D CT

Sathish Ramani and Jeffrey A. Fessler

***Abstract*—Statistical reconstruction methods for X-ray CT rely on regularization to yield good quality images. We propose and investigate a specific type of nonquadratic regularization for 3-D CT reconstruction that corresponds to applying a 2-D orthonormal wavelet transform (OWT) on trans-axial slices and finite differences (FD) along the axial direction. We use an iterative variable-splitting-based *alternating direction method of multipliers* (ADMM) reconstruction algorithm that effectively handles the proposed regularizer. We also present a simple procedure to incorporate iteration-dependent random shifting to circumvent the shift-variance of OWT and to reduce block artifacts. The proposed regularizer requires less memory compared to those that use FDs and is thus advantageous for ADMM that stores and manipulates auxiliary variables related to the regularizer. We demonstrate using simulation with a 3-D XCAT phantom that the proposed regularizer yields images that are visually comparable in quality to those obtained using a regularizer composed of FDs.**

***Index Terms*—X-ray CT imaging, statistical image reconstruction, nonquadratic regularization, alternating direction method of multipliers, orthonormal wavelet transform.**

I. Introduction

Regularized reconstruction methods for X-ray CT can provide good image quality at the expense of increased computation compared to unregularized noniterative methods such as FBP. Nonquadratic regularizers that preserve edges [1] or those that promote sparsity are particularly appealing for CT reconstruction [2]. Such regularizers are usually composed of shift-invariant operators such as finite differences (FD) [1] or frames [2]. Wavelet frames are especially attractive due to their multiresolution nature and have been employed for CT [2], [3]; they may also be interpreted as multiresolution extensions of finite differences. However, for 3-D CT, frames can increase computation (due to calculation of frame coefficients during reconstruction) compared to FDs and would require a significant memory overhead when used with some algorithms like *iterative shrinkage thresholding* (IST) [4], [5] or *alternating direction method of multipliers* (ADMM) [2].

An orthonormal wavelet transform (OWT) is a computation- and memory-efficient alternative to a wavelet frame. OWTs retain the multiresolution aspect of wavelet frames and have been successfully used in reconstruction problems in image processing [4] and magnetic resonance imaging [5]. In this work, we investigate the use of OWT for 3-D CT reconstruction. Specifically, we propose a hybrid nonquadratic regularizer that is composed of 2-D OWTs (applied on the trans-axial slices) and FDs (applied along the axial direction). We used the ADMM algorithm [2], for performing reconstruction as it can easily handle the proposed regularizer. Based on our previous work [6], we also present a simple strategy to integrate iteration-dependent random shifting (IDRS) in ADMM to compensate for the shift-variance of OWT and to reduce block-artifacts therefrom. We illustrate using simulations with a 3-D XCAT phantom [7] that the proposed approach is able to provide reconstruction results that are qualitatively similar to those obtained using a regularizer with FDs. Our method can be easily extended for use with 3-D OWTs and can be readily applied to axial and helical CT.

This work was supported by the National Institutes of Health under Grant R01-HL-098686.

Sathish Ramani and Jeffrey A. Fessler are with the Electrical Engineering and Computer Science Department, University of Michigan, Ann Arbor, MI, USA.

II. Statistical X-ray CT Reconstruction

A. Problem Formulation

We consider a penalized weighted least-squares formulation of statistical 3-D X-ray CT reconstruction [1],

$$\arg\min_{\mathbf{x}} \left\{ \frac{1}{2}\|\mathbf{y} - \mathbf{A}\mathbf{x}\|_{\mathbf{W}}^2 + \Psi(\boldsymbol{\mathcal{B}}\mathbf{x}) \right\}, \tag{1}$$

where $\mathbf{x} \in \mathbb{R}^N$ is a vector representing the 3-D volume (of size $N = N_1 \times N_2 \times N_3$) being reconstructed, $\mathbf{y} \in \mathbb{R}^M$ is the logarithm of raw transmission data, $\mathbf{W} \in \mathbb{R}_+^{M \times M}$ is a diagonal matrix consisting of statistical weights [1], [2], $\mathbf{A} \in \mathbb{R}^{M \times N}$ is the system matrix so that $\mathbf{A}\mathbf{x}$ represents line integrals. We consider a regularizer of the form

$$\Psi(\boldsymbol{\mathcal{B}}\mathbf{x}) = \lambda \sum_r \kappa_r \Phi(|[\boldsymbol{\mathcal{B}}\mathbf{x}]_r|), \tag{2}$$

where $\boldsymbol{\mathcal{B}}$ represents the regularization operator, Φ is a potential function, $\lambda > 0$ is the regularization parameter and $\kappa_r > 0$ are weights that govern the spatial resolution [8] in the reconstructed result.

B. Regularization Operator

While common choices for $\boldsymbol{\mathcal{B}}$ in 3-D CT are finite differences (FD) along 3 orthogonal directions, or more comprehensively, along 13 nearest-neighbor-directions [1], we explore the use of an orthonormal wavelet transform (OWT) for (1) in this work. OWTs posses several attractive properties including regularity, sparsity / compressibility and their ability to represent an image at multiple scales and have been widely used in image-processing applications, e.g., restoration [4], and magnetic resonance image reconstruction [5]. There are several ways to incorporate OWTs for 3-D CT reconstruction, e.g., one could consider (a) an entirely wavelet-based regularizer using a 3-D OWT, or (b) some combination of OWTs and FDs for $\boldsymbol{\mathcal{B}}$ in (2). The advantage of (b) is that it allows for simultaneous utilization of wavelet-properties and shift-invariance of FDs,

so we specifically choose to investigate the following hybrid-form for $\boldsymbol{\mathcal{B}}$:

$$\boldsymbol{\mathcal{B}} = \begin{bmatrix} \boldsymbol{\mathcal{V}} \\ \boldsymbol{\mathcal{C}} \end{bmatrix}, \tag{3}$$

where $\boldsymbol{\mathcal{V}} = \mathbf{I}_{N_3} \otimes \boldsymbol{\mathcal{W}}$, $\boldsymbol{\mathcal{C}} = \mathbf{R} \otimes \mathbf{I}_{N_1 N_2}$, $\otimes$ represents Kronecker product, and $\mathbf{I}_M$ is the identity matrix of size M. The operator $\boldsymbol{\mathcal{B}}$ in (3) thus corresponds to applying a 2-D OWT, represented by $\boldsymbol{\mathcal{W}} \in \mathbb{R}^{N_1 N_2 \times N_1 N_2}$, on each trans-axial slice and nearest-neighbor-differences, represented by $\mathbf{R} \in \mathbb{R}^{N_3 \times N_3}$, along the axial direction (perpendicular to the trans-axial slices). Moreover, as the axial direction is handled separately in $\boldsymbol{\mathcal{B}}$ (3), it allows for the use of varying regularization strength along that direction to account for the cylindrical nature of CT scanner geometries [1].

III. A Splitting-Based Iterative Method

IST-type algorithms [4], [5] are a common choice for solving inverse problems like (1) with entirely wavelet-based regularizers. However, the inclusion of FDs in $\boldsymbol{\mathcal{B}}$ (3) precludes the use of IST-type algorithms for (1). Gradient-descent algorithms like nonlinear conjugate gradient (NCG) can be readily applied for (1), but they are difficult to precondition due to the highly shift-variant nature of the Hessian, $\mathbf{A}^\top \mathbf{W} \mathbf{A}$, of the data-fidelity term in (1) [2] and thus may converge slowly.

Recently, we proposed an iterative variable-splitting-based ADMM algorithm [2] for solving (1). ADMM employs auxiliary constraint variables to separate $\mathbf{A}$ from the data-fidelity term and $\boldsymbol{\mathcal{B}}$ from the regularization term in (1) [2]. The resulting effect of these variables is that ADMM involves simple update steps [2] that correspond to inverting a diagonal matrix, minimizing 1-D denoising cost functions that can be achieved analytically and solving a linear system of equations that is amenable to iterative solvers (e.g., preconditioned conjugate gradient) with effective preconditioning using circulant matrices (e.g., associated with cone-type filters [2]). These features enable fast convergence of ADMM compared to contemporary methods for CT [2] and also allow it to tackle a variety of regularization criteria [2] including the proposed one (2)-(3).

A. ADMM Algorithm

For solving (1) using ADMM, we employ constraints of the form $\mathbf{u} = \mathbf{A}\mathbf{x}$ and $\mathbf{v} = \boldsymbol{\mathcal{B}}\mathbf{x}$, where for ease of analysis, we decompose $\mathbf{v} = [\mathbf{v}_1^\top \mathbf{v}_2^\top]^\top$, so that $\mathbf{v}_1 = \boldsymbol{\mathcal{V}}\mathbf{x}$ and $\mathbf{v}_2 = \boldsymbol{\mathcal{C}}\mathbf{x}$ for $\boldsymbol{\mathcal{B}}$ in (3). Through a derivation similar to that in [2, Sec. III], we obtain the following ADMM algorithm, where at iteration j, we perform the following sequence of operations:

$$\mathbf{x}^{(j+1)} = \mathbf{G}_\nu^{-1} \left(\begin{array}{l} \mathbf{A}^\top (\mathbf{u}^{(j)} - \boldsymbol{\eta}_{\mathbf{u}}^{(j)}) \\ \quad + \nu \boldsymbol{\mathcal{V}}^\top (\mathbf{v}_1^{(j)} - \boldsymbol{\eta}_{\mathbf{v}_1}^{(j)}) \\ \quad + \nu \boldsymbol{\mathcal{C}}^\top (\mathbf{v}_2^{(j)} - \boldsymbol{\eta}_{\mathbf{v}_2}^{(j)}) \end{array} \right), \tag{4}$$

$$\mathbf{u}^{(j+1)} = \mathbf{D}_\mu^{-1} (\mathbf{W}\mathbf{y} + \mu [\mathbf{A}\mathbf{x}^{(j+1)} + \boldsymbol{\eta}_{\mathbf{u}}^{(j)}]), \tag{5}$$

$$\mathbf{v}_1^{(j+1)} = \arg\min_{\mathbf{v}_1} \left\{ \Psi(\mathbf{v}_1) + \frac{\mu\nu}{2} \left\| \mathbf{v}_1 - [\boldsymbol{\mathcal{V}}\mathbf{x}^{(j+1)} + \boldsymbol{\eta}_{\mathbf{v}_1}^{(j)}] \right\|_2^2 \right\}, \tag{6}$$

$$\mathbf{v}_2^{(j+1)} = \arg\min_{\mathbf{v}_2} \left\{ \Psi(\mathbf{v}_2) + \frac{\mu\nu}{2} \left\| \mathbf{v}_2 - [\boldsymbol{\mathcal{C}}\mathbf{x}^{(j+1)} + \boldsymbol{\eta}_{\mathbf{v}_2}^{(j)}] \right\|_2^2 \right\}, \tag{7}$$

$$\boldsymbol{\eta}_{\mathbf{u}}^{(j+1)} = \boldsymbol{\eta}_{\mathbf{u}}^{(j)} - (\mathbf{u}^{(j+1)} - \mathbf{A}\mathbf{x}^{(j+1)}), \tag{8}$$

$$\boldsymbol{\eta}_{\mathbf{v}_1}^{(j+1)} = \boldsymbol{\eta}_{\mathbf{v}_1}^{(j)} - (\mathbf{v}_1^{(j+1)} - \boldsymbol{\mathcal{V}}\mathbf{x}^{(j+1)}), \tag{9}$$

$$\boldsymbol{\eta}_{\mathbf{v}_2}^{(j+1)} = \boldsymbol{\eta}_{\mathbf{v}_2}^{(j)} - (\mathbf{v}_2^{(j+1)} - \boldsymbol{\mathcal{C}}\mathbf{x}^{(j+1)}). \tag{10}$$

The Lagrange-multiplier-like vectors $\boldsymbol{\eta}_{\mathbf{u}}^{(\cdot)}$, $\boldsymbol{\eta}_{\mathbf{v}_1}^{(\cdot)}$ and $\boldsymbol{\eta}_{\mathbf{v}_2}^{(\cdot)}$ are associated with the constraint variables $\mathbf{u}$, $\mathbf{v}_1$ and $\mathbf{v}_2$, respectively. The penalty parameters $\mu > 0$, $\nu > 0$ govern only the convergence speed of ADMM and were chosen as described in [2, Sec. III.E], and

$$\mathbf{G}_\nu \triangleq \mathbf{A}^\top \mathbf{A} + \nu(\boldsymbol{\mathcal{V}}^\top \boldsymbol{\mathcal{V}} + \boldsymbol{\mathcal{C}}^\top \boldsymbol{\mathcal{C}}) = \mathbf{A}^\top \mathbf{A} + \nu(\mathbf{I}_N + \boldsymbol{\mathcal{C}}^\top \boldsymbol{\mathcal{C}}), \tag{11}$$

where we have used the orthonormality of $\boldsymbol{\mathcal{W}}$ and $\boldsymbol{\mathcal{V}}$ in (11):

$$\boldsymbol{\mathcal{W}}^\top \boldsymbol{\mathcal{W}} = \boldsymbol{\mathcal{W}} \boldsymbol{\mathcal{W}}^\top = \mathbf{I}_{N_1 N_2} \implies \boldsymbol{\mathcal{V}}^\top \boldsymbol{\mathcal{V}} = \boldsymbol{\mathcal{V}} \boldsymbol{\mathcal{V}}^\top = \mathbf{I}_N. \tag{12}$$

Since $\mathbf{A}^\top \mathbf{A}$ is "more" shift-invariant than $\mathbf{A}^\top \mathbf{W} \mathbf{A}$ [2] and because $\boldsymbol{\mathcal{C}}^\top \boldsymbol{\mathcal{C}} = \mathbf{R}^\top \mathbf{R} \otimes \mathbf{I}_{N_1 N_2}$ is shift-invariant ($\mathbf{R}$ is a finite differencing matrix), a CG-solver for (4) is amenable to FFT-based preconditioning using suitable cone-type filters [2]. The updates corresponding to $\boldsymbol{\eta}_{\mathbf{u}}^{(\cdot)}$, $\boldsymbol{\eta}_{\mathbf{v}_1}^{(\cdot)}$, $\boldsymbol{\eta}_{\mathbf{v}_2}^{(\cdot)}$ (8)-(10) are trivial. The matrix $\mathbf{D}_\mu \triangleq \mathbf{W} + \mu \mathbf{I}_M$ is diagonal and can be inverted exactly in (5).

The minimizations in (6)-(7) each decouple in to $2N$ scalar denoising problems in terms of the components $\{v_{i,r}\}_{r=1}^N$ of $\mathbf{v}_i$, $i = 1, 2$, for the regularization Ψ in (2). Writing, $\boldsymbol{\varrho}_{\mathbf{v}_1}^{(j)} \triangleq \boldsymbol{\mathcal{V}}\mathbf{x}^{(j+1)} + \boldsymbol{\eta}_{\mathbf{v}_1}^{(j)}$, $\boldsymbol{\varrho}_{\mathbf{v}_2}^{(j)} \triangleq \boldsymbol{\mathcal{C}}\mathbf{x}^{(j+1)} + \boldsymbol{\eta}_{\mathbf{v}_2}^{(j)}$, we have that

$$v_{i,r}^{(j+1)} = \arg\min_v \left\{ \Psi(v) + \frac{\mu\nu}{2} (v - \varrho_{\mathbf{v}_i,r}^{(j)})^2 \right\}, \tag{13}$$

$\varrho_{\mathbf{v}_i,r}^{(j)}$ is the r-th component of $\boldsymbol{\varrho}_{\mathbf{v}_i}^{(j)}$, $i = 1, 2$, $r = 1, \ldots, N$. The 1-D problem (13) admits analytical closed-form solution for a variety of potential functions Φ [2]. For simplicity, we focus on the Fair potential (smoothed-Laplacian)

$$\Phi(x) = \Phi_{\mathrm{FP}}(x) \triangleq x/\delta - \log(1 + x/\delta), \tag{14}$$

$\delta > 0$, that has been used successfully for CT [2], [6]. For Φ_{FP}, (13) leads to [2]

$$v_{i,r}^{(j+1)} = \mathrm{sign}\{\varrho_{\mathbf{v}_i,r}^{(j)}\} \frac{\zeta_{\mathbf{v}_i,r}^{(j)} + \sqrt{(\zeta_{\mathbf{v}_i,r}^{(j)})^2 + 4\delta |\varrho_{\mathbf{v}_i,r}^{(j)}|}}{2}, \tag{15}$$

where $\zeta_{\mathbf{v}_i,r}^{(j)} \triangleq |\varrho_{\mathbf{v}_i,r}^{(j)}| - \delta - \lambda \kappa_r / (\delta \mu \nu)$, $i = 1, 2$.

B. Memory Requirement

Compared to other iterative methods like NCG or IST-type algorithms, ADMM requires more memory as it needs to store $\mathbf{u}^{(\cdot)}$, $\mathbf{v}^{(\cdot)}$ and associated Lagrange-multiplier-like vectors. Depending on the regularization, memory requirement for $\mathbf{v}^{(\cdot)}$ may overshoot that of $\mathbf{u}^{(\cdot)}$ and represent a significant memory-overhead for 3-D CT; this is particularly the case with FDs when all 13 nearest-neighbour directions are used [2]. As an alternative, FDs in 3 orthogonal directions may be considered, which will only require a total of 6 image-volumes for storing $\mathbf{v}^{(\cdot)}$ and its Lagrange-multiplier vector (significantly less than 26 image-volumes required for the 13-neighborhood case). In comparison, ADMM for the proposed regularization operator $\boldsymbol{\mathcal{B}}$ (3) requires even less memory, a total of only 4 image-volumes for storing $\mathbf{v}^{(\cdot)}$ and its Lagrange-multiplier vector, due to the use of the OWT $\boldsymbol{\mathcal{W}}$ in $\boldsymbol{\mathcal{B}}$; the proposed $\boldsymbol{\mathcal{B}}$ (3) is thus advantageous for ADMM-based 3-D CT reconstruction.

IV. Iteration-Dependent Random Shifting

Memory efficiency of an OWT comes at the expense of its shift-variant nature that can lead to block-artifacts in the reconstructed image [5], [6]. Iteration dependent random shifting (IDRS) [4] is a cost-effective technique for partially compensating the shift-variance of OWT and has been successfully used for image restoration [4] and MRI reconstruction [5] with iterative shrinkage-thresholding (IST) type methods. We proposed a simple strategy recently to incorporate IDRS in ADMM for statistical 2-D CT reconstruction using regularization composed entirely of OWT [6]. The basic idea there is to apply an iteration-varying random translation to the estimate $\mathbf{x}^{(j)}$ before solving a denoising problem akin to (6) and then to undo the translation later in the sequence of updates in ADMM. The same idea can be readily extended to the OWT-part of the proposed $\boldsymbol{\mathcal{B}}$ (3) and the update equation (6) for corresponding constraint variable $\mathbf{v}_1$.

Before proceeding, it is useful to introduce $\widetilde{\mathbf{v}}_1 \triangleq \boldsymbol{\mathcal{V}}^\top \mathbf{v}_1$ and $\boldsymbol{\eta}_{\widetilde{\mathbf{v}}_1} \triangleq \boldsymbol{\mathcal{V}}^\top \boldsymbol{\eta}_{\mathbf{v}_1}$. Then the updates that depend on $\boldsymbol{\mathcal{V}}$, (4), (6) and (9), respectively, become

$$\mathbf{x}^{(j+1)} = \mathbf{G}_\nu^{-1} \begin{pmatrix} \mathbf{A}^\top(\mathbf{u}^{(j)} - \boldsymbol{\eta}_{\mathbf{u}}^{(j)}) & +\nu(\widetilde{\mathbf{v}}_1^{(j)} - \boldsymbol{\eta}_{\widetilde{\mathbf{v}}_1}^{(j)}) \\ & +\nu \boldsymbol{\mathcal{C}}^\top(\mathbf{v}_2^{(j)} - \boldsymbol{\eta}_{\mathbf{v}_2}^{(j)}) \end{pmatrix}, \quad (16)$$

$$\widetilde{\mathbf{v}}_1^{(j+1)} = \boldsymbol{\mathcal{V}}^\top \left(\arg\min_{\mathbf{v}_1} \left\{ \begin{array}{l} \Psi(\mathbf{v}_1) + \\ \frac{\mu\nu}{2} \left\| \mathbf{v}_1 - \boldsymbol{\mathcal{V}}[\mathbf{x}^{(j+1)} + \widetilde{\boldsymbol{\eta}}_{\mathbf{v}_1}^{(j)}] \right\|_2^2 \end{array} \right\} \right), \quad (17)$$

$$\boldsymbol{\eta}_{\widetilde{\mathbf{v}}_1}^{(j+1)} = \boldsymbol{\eta}_{\widetilde{\mathbf{v}}_1}^{(j)} - (\widetilde{\mathbf{v}}_1^{(j+1)} - \mathbf{x}^{(j+1)}), \quad (18)$$

where we have used the orthonormality of $\boldsymbol{\mathcal{V}}$ in (17) and (18). Thus the only step in ADMM where $\boldsymbol{\mathcal{V}}$ (i.e., OWT) appears now is (17), so we need only focus on (17) for incorporating IDRS. Since we want to promote shift-invariance, at each iteration j, we consider $\boldsymbol{\mathcal{S}}^{(j)} \triangleq \mathrm{diag}\{\boldsymbol{\mathcal{S}}_1^{(j)} \cdots \boldsymbol{\mathcal{S}}_{N_3}^{(j)}\}$, where $\{\boldsymbol{\mathcal{S}}_i^{(j)}\}_{i=1}^{N_3}$ are $N_1N_2 \times N_1N_2$ block permutation matrices, such that the action of $\boldsymbol{\mathcal{S}}^{(j)}$ on $\mathbf{x}^{(j)}$ randomly translates each trans-axial slice by different amounts. Then applying IDRS simply amounts to using $\widetilde{\boldsymbol{\mathcal{V}}}^{(j)} \triangleq \boldsymbol{\mathcal{V}}\boldsymbol{\mathcal{S}}^{(j)}$ in (17), i.e., $\widetilde{\mathbf{v}}_1^{(j+1)} =$

$$\widetilde{\boldsymbol{\mathcal{V}}}^{(j)\top} \left(\arg\min_{\mathbf{v}_1} \left\{ \begin{array}{l} \Psi(\mathbf{v}_1) + \\ \frac{\mu\nu}{2} \left\| \mathbf{v} - \widetilde{\boldsymbol{\mathcal{V}}}^{(j)}[\mathbf{x}^{(j+1)} + \widetilde{\boldsymbol{\eta}}_{\mathbf{v}_1}^{(j)}] \right\|_2^2 \end{array} \right\} \right), \quad (19)$$

that is, IDRS is first applied to the input $(\mathbf{x}^{(j+1)} + \widetilde{\boldsymbol{\eta}}_{\mathbf{v}_1}^{(j)})$ to the denoising step (19) via $\widetilde{\boldsymbol{\mathcal{V}}}^{(j)}$, the denoising operation [minimization in (19)] is performed similar to (13)-(15), and IDRS is undone later in the same step via $\widetilde{\boldsymbol{\mathcal{V}}}^{(j)\top}$. This is similar to how IDRS is also applied in IST-type algorithms [4], [5]. We summarize below our ADMM-IDRS scheme for 3-D CT reconstruction assuming we have a sequence of random translations represented by $\{\boldsymbol{\mathcal{S}}^{(j)}\}$.

ADMM-IDRS for 3-D CT Reconstruction

1. Initialization: $\mathbf{x}^{(1)}$; Set $\boldsymbol{\eta}_{\mathbf{u}}^{(0)} = \boldsymbol{\eta}_{\widetilde{\mathbf{v}}_1}^{(0)} = \boldsymbol{\eta}_{\mathbf{v}_2}^{(0)} = \boldsymbol{\eta}_{\mathbf{u}}^{(1)} = \boldsymbol{\eta}_{\widetilde{\mathbf{v}}_1}^{(1)} = \boldsymbol{\eta}_{\mathbf{v}_2}^{(1)} = \mathbf{0}$; Compute $\mathbf{u}^{(1)}$ using (5); obtain $\widetilde{\mathbf{v}}_1^{(1)}$, $\mathbf{v}_2^{(1)}$, respectively, using (19), (7), (13)-(15); set $j = 1$.
2. Apply (P)CG for partially solving (16) to obtain $\mathbf{x}^{(j+1)}$.
3. Compute $\mathbf{u}^{(j+1)}$ using (5).
4. Obtain $\widetilde{\mathbf{v}}_1^{(j+1)}$, $\mathbf{v}_2^{(j+1)}$ using (19), (7) and (13)-(15).
5. Update $\boldsymbol{\eta}_{\mathbf{u}}^{(j+1)}$, $\boldsymbol{\eta}_{\widetilde{\mathbf{v}}_1}^{(j+1)}$, $\boldsymbol{\eta}_{\mathbf{v}_2}^{(j+1)}$ using (8), (18), (10).
6. Set $j \leftarrow j+1$; Repeat Steps 2-6 till stop criterion is met.

IDRS as applied to ADMM above for 3-D CT reconstruction is computationally efficient since it only requires trivial translation operations and provides image quality comparable to that obtained using FDs as demonstrated next.

V. Experimental Setup & Results

We performed simulations with a 3-D XCAT phantom [7] of size $1024 \times 1024 \times 188$. We generated a $888 \times 984 \times 64$ noisy sinogram with GE LightSpeed fan-beam geometry [2] (axial scan) corresponding to a monoenergetic source with 5×10^5 incident photons per ray and no background events. We reconstructed $512 \times 512 \times 92$ image-volumes (that include a padding of 28 trans-axial slices to account for the "long object problem" of the scanner geometry) whose trans-axial FOV was 50 cm and whose axial FOV of the region of interest was 4 cm. We used the separable-footprints (SF-TR) projector [9] (implemented in C) for computing matrix-vector products such as $\mathbf{Ax}$, $\mathbf{A}^\top\mathbf{u}$ and initialized ADMM [2] and the proposed ADMM-IDRS with the image-volume reconstructed using FDK with Hanning filter. We applied 5 CG iterations with a cone-filter-type preconditioner [2] for "solving" (16). We compared reconstruction quality yielded by the regularizer in (2) with Φ_{FP} [$\delta = 10$ HU (14)] using (a) finite differences (FD) in 3 orthogonal directions and (b) the proposed operator $\boldsymbol{\mathcal{B}}$ (3) employing 3 levels of the orthonormal Haar wavelet transform for $\boldsymbol{\mathcal{W}}$. Computation times of ADMM [2] for case (a) and the proposed ADMM-IDRS for case (b) were dominated by products with $\mathbf{A}$ and $\mathbf{A}^\top$ and were similar ($\approx$ 3 minutes / iteration in Matlab running on a 12-core PC with 2.80 GHz Intel Xeon CPUs and 24 GB RAM).

We set $\kappa_r = \sqrt{[\mathbf{A}^\top\mathbf{W}\mathbf{1}]_r / [\mathbf{A}^\top\mathbf{1}]_r}$ [8] wherever FDs were involved (including those in $\boldsymbol{\mathcal{B}}$). For the OWT part in $\boldsymbol{\mathcal{B}}$, we first applied IDRS, i.e., $\boldsymbol{\mathcal{S}}^{(\cdot)}$, to $\boldsymbol{\kappa} = \{\kappa_r\}$ and propagated the resulting vector through the wavelet decomposition tree without employing the wavelet-filtering steps to obtain a set of subband-dependent weights that replaced κ_r in (15) for ($i = 1$) the OWT part of $\boldsymbol{\mathcal{B}}$. We also set the weights corresponding to the approximation coefficients to zero (i.e., they were not thresholded since they are not sparse in general [4]–[6]). We chose the regularization parameter λ so as to roughly compromise between smoothing and reduction of noise and artifacts. Figs. 1-3 present reconstruction results for our simulation. Both regularized reconstruction results (third and fourth columns in all figures) provide improved quality over the FDK result along the trans-axial, coronal and sagittal views. Moreover, the proposed method [ADMM-IDRS with $\boldsymbol{\mathcal{B}}$ (3)] yields reconstructed images (fourth column in Figs. 1-3) that are visually comparable to those obtained using finite differences in 3 orthogonal directions (third column in Figs. 1-3) indicating the potential of orthonormal wavelets and IDRS for 3-D CT reconstruction.

VI. Conclusion & Discussion

We proposed a hybrid nonquadratic regularizer (2) for statistical 3-D CT reconstruction with an operator $\boldsymbol{\mathcal{B}}$ (3) that applies a 2-D orthonormal wavelet transform (OWT) on trans-axial

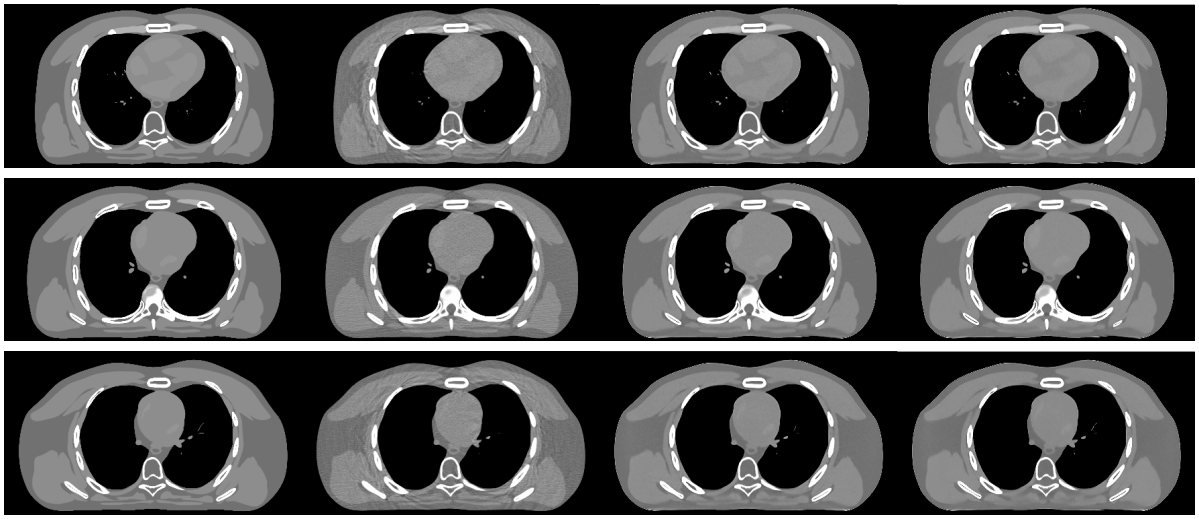

Fig. 1. Simulation with a 3-D XCAT phantom. Zoomed slices in **trans-axial view** (444×242). **First row:** Slice 26, **Second row:** Slice 46 and **Third row:** Slice 66. **First column:** Noisefree phantom; **Second column:** FDK result with Hanning filter; **Third column:** ADMM result for Φ_{FP} (14) with finite differences in 3 orthogonal directions; **Fourth column:** ADMM-IDRS result for Φ_{FP} (14) with proposed operator $\mathcal{B}$ (3) involving OWT. Images are displayed in Hounsfield units in the range of [800, 1200].

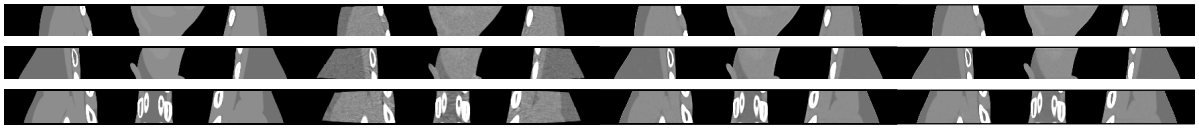

Fig. 2. Simulation with a 3-D XCAT phantom. Zoomed slices in **coronal view** (444×50). **First row:** Slice 197, **Second row:** Slice 257 and **Third row:** Slice 317. **First column:** Noisefree phantom; **Second column:** FDK result with Hanning filter; **Third column:** ADMM result for Φ_{FP} (14) with finite differences in 3 orthogonal directions; **Fourth column:** ADMM-IDRS result for Φ_{FP} (14) with proposed operator $\mathcal{B}$ (3) involving OWT. Images are displayed in Hounsfield units in the range of [800, 1200].

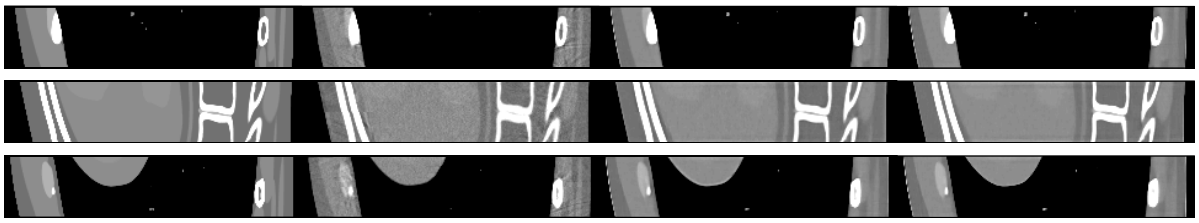

Fig. 3. Simulation with a 3-D XCAT phantom. Zoomed slices in **sagittal view** (242×50). **First row:** Slice 197, **Second row:** Slice 257 and **Third row:** Slice 317. **First column:** Noisefree phantom; **Second column:** FDK result with Hanning filter; **Third column:** ADMM result for Φ_{FP} (14) with finite differences in 3 orthogonal directions; **Fourth column:** ADMM-IDRS result for Φ_{FP} (14) with proposed operator $\mathcal{B}$ (3) involving OWT. Images are displayed in Hounsfield units in the range of [800, 1200].

slices and finite differences (FD) along the axial direction. We developed a simple scheme to incorporate iteration-dependent random shifting (IDRS) [4]–[6] in the ADMM reconstruction algorithm [2] to compensate for the shift-variance of the OWT part of the proposed operator $\mathcal{B}$ (3). Simulations with a 3-D XCAT phantom indicate that the proposed method, i.e., ADMM-IDRS with the hybrid regularizer (2)-(3), yields reconstructed images that are qualitatively similar to those obtained using a regularizer composed of FDs in 3 orthogonal directions. We are currently evaluating improved choices for subband-dependent weights for the OWT part of the proposed regularizer (2)-(3). The next step is to compare the proposed regularizer (2)-(3) against one that uses FDs in all 13 nearest-neighbour directions [1] in 3-D. We also plan to investigate regularization criteria that use 3-D OWT for 3-D CT reconstruction with application to helical CT.

REFERENCES

[1] J-B. Thibault, K. Sauer, C. Bouman, and J. Hsieh, "A three-dimensional statistical approach to improved image quality for multi-slice helical CT," *Med. Phys.*, vol. 34, no. 11, pp. 4526–44, Nov. 2007.

[2] S. Ramani and J. A. Fessler, "A splitting-based iterative algorithm for accelerated statistical X-ray CT reconstruction," *IEEE Trans. Med. Imag.*, vol. 3, no.3, pp. 677–88, Mar. 2012.

[3] X. Jia, B.Dong, Y.Lou, and S. B. Jiang, "GPU-based iterative cone-beam CT reconstruction using tight frame regularization," *Phys. Med. Biol.*, vol. 56, pp. 3787–807, 2011.

[4] M. A. T. Figueiredo and R. D. Nowak, "An EM algorithm for wavelet-based image restoration," *IEEE Trans. Im. Proc.*, vol. 12, no. 8, pp. 906–16, Aug. 2003.

[5] M. Guerquin-Kern, M. Haberlin, K.P. Pruessmann, and M. Unser, "A fast wavelet-based reconstruction method for magnetic resonance imaging," *IEEE Trans. Med. Imag.*, vol. 30, no. 9, pp. 1649–1660, 2011.

[6] S. Ramani and J. A. Fessler, "Statistical X-ray CT reconstruction using a splitting-based iterative algorithm with orthonormal wavelets," *Proc. IEEE Intl. Symp. Biomed. Imag.*, pp. 1008-11, Barcelona, Spain, 2012.

[7] W. P. Segars, M. Mahesh, T. J. Beck, E. C. Frey, and B. M. W. Tsui, "Realistic CT simulation using the 4D XCAT phantom," *Med. Phys.*, vol. 35, no. 8, pp. 3800–8, Aug. 2008.

[8] J. A. Fessler and W. L. Rogers, "Spatial resolution properties of penalized-likelihood image reconstruction methods: Space-invariant tomographs," *IEEE Trans. Im. Proc.*, vol. 5, no. 9, pp. 1346–58, Sept. 1996.

[9] Y. Long, J. A. Fessler, and J. M. Balter, "3D forward and back-projection for X-ray CT using separable footprints," *IEEE Trans. Med. Imag.*, vol. 29, no. 11, pp. 1839–50, Nov. 2010.